



RESEARCH LETTER

10.1002/2017GL073662

Key Points:

- A diagnostic for detecting atmospheric fronts objectively is introduced
- Diagnostic includes both a thermal and dynamical component
- A comparison with a more traditional thermal-only method is presented

Supporting Information:

- Supporting Information S1

Correspondence to:

R. Parfitt,
rparfitt@whoi.edu

Citation:

Parfitt, R., A. Czaja, and H. Seo (2017), A simple diagnostic for the detection of atmospheric fronts, *Geophys. Res. Lett.*, 44, doi:10.1002/2017GL073662.

Received 29 MAR 2017

Accepted 20 APR 2017

Accepted article online 24 APR 2017

A simple diagnostic for the detection of atmospheric fronts

Rhys Parfitt^{1,2} , Arnaud Czaja², and Hyodae Seo¹ ¹Department of Physical Oceanography, Woods Hole Oceanographic Institution, Woods Hole, Massachusetts, USA,²Department of Physics, Imperial College London, London, UK

Abstract In this article, a simple diagnostic to identify atmospheric fronts objectively from gridded data sets is presented. For this diagnostic, fronts are identified as regions where the normalized product of the isobaric relative vorticity and horizontal temperature gradient exceeds a threshold value. The purpose is to introduce a method that is both robust and particularly straightforward in calculation. A climatology of atmospheric fronts, as well as the identification of an individual frontal system, is computed using this diagnostic. These are subsequently compared to a more traditional frontal detection method and the similarities and differences discussed.

1. Introduction

It has long been understood that extratropical cyclones and the frontal systems embedded in them are responsible for much of the rainfall in the middle latitudes [Bjerknes and Solberg, 1922; Hawcroft et al., 2012; Catto et al., 2012]. Indeed, frontal rainfall contributes significantly to extreme precipitation events, with up to 90% of extreme precipitation events in the midlatitudes associated with fronts [Catto and Pfahl, 2013]. As such, the passing of frontal systems has major socioeconomic influence, and their identification is of crucial importance.

Traditionally, detection of atmospheric fronts has involved using the *thermal front parameter* (TFP) [Renard and Clarke, 1965; Clarke and Renard, 1966; Huber-Pock and Kress, 1981, 1989], a diagnostic quantity based on a chosen variable (usually related to temperature) on a certain atmospheric pressure level. Maxima, minima, or threshold regions of this diagnostic are identified as frontal, before the application of additional masking criteria. However, the actual methods of identification have usually required at least some degree of manual (i.e., human) input. Naturally, the potential benefits of fully automating frontal detection are numerous (for an extensive discussion, see Hewson [1998]—hereafter H98). While several methods have been proposed that invoke fully automated processes [e.g., Japan Meteorological Agency, 1988], these have generally involved nontrivial algorithms. Currently, most studies that require automatic objective frontal identification follow a method based on the work of H98, where threshold values of a chosen diagnostic are masked subject to threshold criteria on the TFP [e.g., Berry et al., 2011a, 2011b; Catto and Pfahl, 2013].

Nevertheless, there are distinct methods of frontal identification in use, such as that introduced in Simmonds et al. [2012], which employs a dynamical diagnostic based on temporal changes in the 10 m wind. A direct comparison of this method with that of H98 is presented in Schemm et al. [2015], as well as other potential methods in a case study by Hope et al. [2014]. These studies highlight an important aspect of frontal detection in that there is actually no widely accepted definition of an atmospheric front, which can often lead to noticeable differences in meteorological studies that employ multiple detection methods. This issue is not restricted to frontal detection and is a common problem often faced within the meteorological community [Neu et al., 2013]. In fact, even within a frontal method itself such as H98, choices will still need to be made based on numerous factors, such as the height considered, the grid spacing of the data set, and chosen threshold values. Indeed, even the techniques for plotting the frontal boundaries themselves can vary [e.g., Hewson, 1998; Jenkner et al., 2010]. It is therefore important to acknowledge that no two frontal detection methods can expect to produce identical results.

In H98, several key requirements are recommended for optimizing objective frontal techniques. Apart from the technique being necessarily *accurate* and *intelligible*, the objective technique should be as *simple* (with minimal differentiation), as *tunable* (whereby fronts are plotted after reaching some threshold intensity), and as *portable* (such that it is easy to apply to any gridded data set) as possible. Furthermore, while

“secondary, nonthermal” variables such as vorticity may characterize certain frontal features, their sole use in frontal definition is cautioned. This article introduces an objective diagnostic that combines one such “nonthermal” variable with a thermal variable, in an attempt to produce a method that meets all of the above criteria, while being highly straightforward in calculation. It is noted that this diagnostic has already been employed in several recent studies [Parfitt, 2014; Sheldon, 2015; Parfitt et al., 2016; Parfitt et al., 2017].

2. Methodology and Data

The data set used in this study is the European Centre for Medium-Range Weather Forecasts Re-Analysis (ERA)-Interim data set [Berrisford et al., 2009]. This data set has spectral resolution T255 ($\sim 0.7^\circ$), is available on a $0.75^\circ \times 0.75^\circ$ longitude-latitude grid, and is used at 6-hourly intervals, across the period 1979–2015.

The frontal variable, F^* , for a particular pressure surface, p , used in this paper is the product of the horizontal temperature gradient on that surface $|\nabla(T_p)|$ with the component of the curl of the wind vector normal to that same pressure surface ζ_p (the isobaric relative vorticity); i.e.,

$$F^* = \zeta_p |\nabla(T_p)|.$$

The basic reasoning for this choice is that in addition to $|\nabla(T_p)|$ being large in frontal situations, so too is ζ_p due to the transverse circulation that develops when cold and warm air masses come together through large-scale confluent flow [Hoskins, 1982; Sheldon, 2015]. Alternative ways of combining $|\nabla(T_p)|$ and ζ_p were trialled, such as the sum of each variable; however, none proved as reliable in our case study analyses. In order to make F^* nondimensional (hereafter denoted by F , the F frontal diagnostic), it is further divided by a typical scale for both the temperature gradient and vorticity,

$$F = F^* / (f|\nabla T|_o),$$

where $|\nabla T|_o = 0.45 \text{ K}/(100 \text{ km})$ and f is the value of the Coriolis parameter at the relevant latitude. As this is a threshold diagnostic, it is important that f is latitude dependent in order to provide a consistent vorticity normalization.

For identification of surface fronts, the pressure level considered is 900 hPa, as recommended in H98. Our normalization values are chosen such that grid points at this level are masked as frontal if F exceeds a threshold value of 1 and have been chosen from an extensive analysis of frontal case studies to provide maximum consistency between objectively masked frontal gridpoints and manual identification. As an example, a grid point will be masked as frontal if a horizontal temperature gradient $|\nabla(T_{900 \text{ hPa}})| = 4.5 \text{ K}/(100 \text{ km})$ is reached simultaneously with an isobaric relative vorticity value of $\zeta_{900 \text{ hPa}} = 0.1f$. “Upper fronts” are also considered at 600 hPa, again following the recommendation in H98. At this level, our case study analyses suggest a threshold value of 2. Masked frontal regions for the F diagnostic can be objectively plotted as regions within contours of these threshold values.

In order to provide a comparison for the F diagnostic, the results presented are illustrated alongside a commonly used frontal detection method following H98. Here for the first masking equation, grid points that satisfy the equation

$$\text{TFP} = -\nabla|\nabla\tau| \cdot \frac{\nabla\tau}{|\nabla\tau|} > K_1,$$

where τ is taken to be the potential temperature, θ , are masked as frontal regions (as used in Booth et al. [2012] and Smirnov et al. [2015] for example). These frontal regions are then subject to the further criterion

$$|\nabla\tau|_{(\text{ABZ})} > K_2,$$

where ABZ signifies the “adjacent baroclinic zone” (cf. H98 for a thorough discussion on the importance of the ABZ). Both K_1 and K_2 are threshold constants to be selected. Following the recommendation in H98, threshold values at 900 hPa are taken as $K_1 = 0.33 \text{ K}(100 \text{ km})^{-2}$ and $K_2 = 1.49 \text{ K}(100 \text{ km})^{-1}$ and at 600 hPa as $K_1 = 0.47 \text{ K}(100 \text{ km})^{-2}$ and $K_2 = 1.41 \text{ K}(100 \text{ km})^{-1}$. This diagnostic will hereafter be referred to as the T diagnostic.

It is noted that the criteria presented for both diagnostics above is for masking individual grid points as “frontal,” and in the case study presented in section 3, no additional criteria are added in order to illustrate

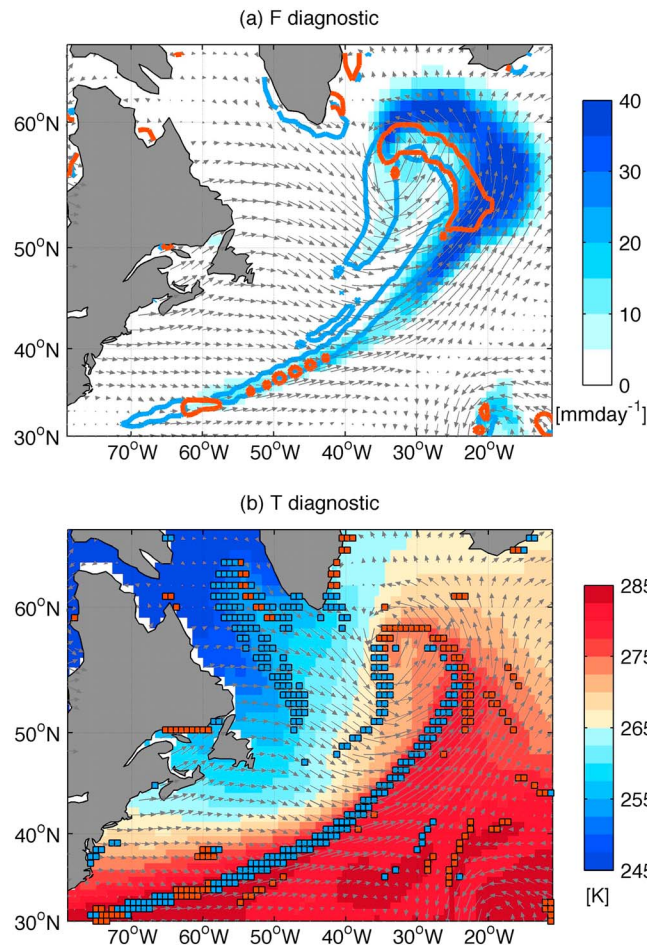


Figure 1. The identification of frontal grid points at 900 hPa in the vicinity of a North Atlantic extratropical cyclone at 0000 UTC on 8 February 1982, as detected by the (a) *F* diagnostic and (b) *T* diagnostic. In Figure 1a, the total precipitation rate is plotted in color in mm d^{-1} , while in Figure 1b the air temperature at 900 hPa is shown in color in K. In both, the instantaneous horizontal wind vectors are included as grey arrows. For the *T* diagnostic, grid points identified as frontal are masked in blue or red depending on whether they are classified as “cold” or “warm” frontal, respectively. For the *F* diagnostic, the grid points identified as frontal are instead plotted as contours of $F = 1$, shaded in blue or red again depending on classification.

across the North Atlantic at 0000 UTC on 8 February 1982, as detected by the *F* diagnostic. The total precipitation in mm d^{-1} is plotted in color, with the instantaneous horizontal wind vectors included as grey arrows. The frontal grid points themselves are objectively plotted here as bounded by contours of $F = 1$, with cold and warm frontal boundaries coloured as blue and red, respectively. Figure 1b illustrates the identification of the same storm, but with the *T* diagnostic. For this figure, the air temperature at 900 hPa is plotted in color, with frontal grid points masked in blue or red depending on their cold or warm classifications, respectively. It is noted that for both diagnostics used in this case study, any frontal grid points with $v_p < 1.5 \text{ m s}^{-1}$ are omitted.

In relation to the air temperature gradient, the band of maximum precipitation, and the instantaneous horizontal wind vectors, both the *F* and *T* diagnostics identify the main cold and warm frontal regions of the extratropical cyclone where one would expect from a manual analysis and there is an excellent degree of agreement between the two. This high level of correspondence in cold and warm frontal regions identified by both diagnostics was also present in multiple case studies performed in the preparation of this manuscript (not shown, although for reference, an additional case study identifying an extratropical cyclone at 0000 UTC

this masking technique. In reality, however, atmospheric fronts themselves have a certain extension, and so in collecting individually masked frontal grid points into fronts, additional criteria must be defined. Unfortunately, as discussed in the introduction, there is no widely accepted definition of what constitutes a front. For example, *Schemm et al.* [2015] require a minimum extension of 500 km, whereas *Berry et al.* [2011a] require there to be at least three contiguous grid points. In section 4, a climatology of atmospheric fronts is produced where two or more neighboring grid points must be masked in order to be considered a front, as used in *Smirnov et al.* [2015].

Frontal grid points for the *F* diagnostic are separated into “cold” and “warm” via calculation of the local geostrophic thermal advection $\mathbf{v}_p \cdot \nabla(T_p)$, where \mathbf{v}_p is the horizontal wind vector on the pressure surface p . The sign of this quantity is positive (negative) for cold (warm) fronts. As used in *Berry et al.* [2011a], a minimum frontal speed v_p of 1.5 m s^{-1} is also required for the cold and warm classifications. For the *T* diagnostic, the classification is instead determined as in *Jenkner et al.* [2010], via the term

$$\mathbf{v}_p \cdot \frac{\nabla T_{\text{TFP}}}{|\nabla T_{\text{TFP}}|}$$

3. A Case Study of an Extratropical Cyclone

Figure 1a illustrates the masked frontal grid points at 900 hPa associated with the passing of an extratropical cyclone

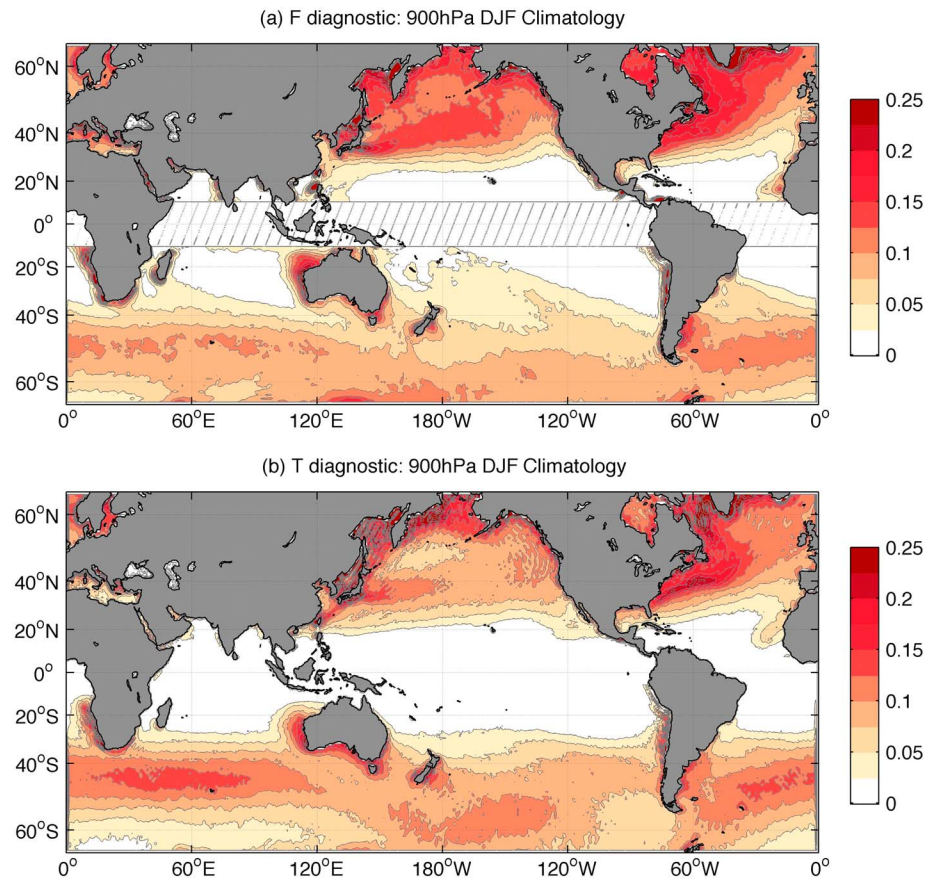


Figure 2. The frequency of all atmospheric fronts at 900 hPa detected using the (a) F diagnostic and (b) T diagnostic, for the Northern Hemisphere wintertime period December–February 1979–2015, expressed as a fraction of the total period.

on 6 August 1981 in the Southern Hemisphere is presented in Figure S1 in the supporting information). These also included analyses of both singular cold and warm fronts of varying zonal and meridional extent.

Nevertheless, it is important to mention that identifications from both diagnostics demonstrate visible differences. These are often regions for which their interpretation as frontal is highly subjective, and several of these can be observed in Figures 1a and 1b. Consider the region over the Labrador Sea, where some grid points are masked as frontal by the T , but not the F , diagnostic. In this region there is a reasonably strong temperature gradient; however, the precipitation and relative vorticity typically associated with an atmospheric front are negligible. Another example can be observed in the bottom right of the domain ($\sim 20^\circ\text{W}$, $\sim 30^\circ\text{N}$). Here frontal grid points are instead masked by the F but not the T diagnostic, where there are noticeable precipitation and relative vorticity patterns. Our analyses have indicated that these differences are especially pronounced for “frontal” regions of little contiguous extension. Often, these types of masked region are removed from analysis due to the application of additional criteria such as a minimum extension requirement, although usually, these criteria will be chosen depending on the user’s specific focus. Unfortunately, differences of this kind between separate frontal diagnostics are common [e.g., Hope *et al.*, 2014], the implications of which are discussed further in sections 4 and 5. This particular case study was chosen to highlight these differences, in addition to demonstrating the similarities in the frontal regions identified within an extratropical cyclone of reasonable spatial extent.

4. Climatology

As mentioned in section 2, singular grid points masked as “frontal” in both diagnostics are removed from the calculation of any climatology in this section to avoid very localized features, as in Smirnov *et al.* [2015]. It is noted that reproducing each climatology illustrated here with a minimum extension of three neighboring

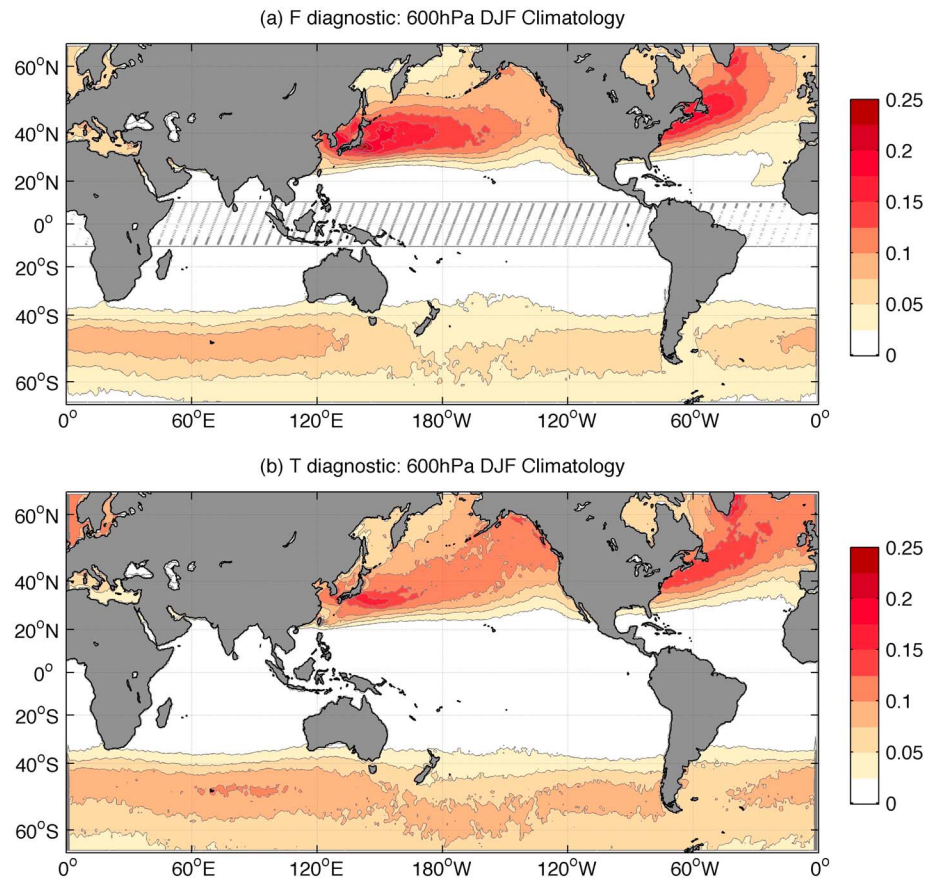


Figure 3. The frequency of all atmospheric fronts at 600 hPa detected using the (a) F diagnostic and (b) T diagnostic, for the Northern Hemisphere wintertime period December–February 1979–2015, expressed as a fraction of the total period.

points required for frontal identification does not in any case significantly change either the magnitude or the structure (not shown).

Figure 2 illustrates the frequency of all atmospheric fronts detected using (a) the F diagnostic and (b) the T diagnostic, respectively, at 900 hPa in Northern Hemisphere (NH) wintertime (taken as December–February, DJF), expressed as a fraction of the total period DJF 1979–2015. For the F diagnostic, the region 10°S to 10°N is masked out due to the convergence of the Coriolis parameter to zero at the equator. This does not affect the present analysis as extremely few fronts are identified at these latitudes, as can be observed in Figure 2b or *Berry et al.* [2011a]. It is acknowledged, however, that this does represent one limitation of using a latitude-dependent normalization in the F diagnostic. For additional reference, an analogous climatology to Figure 2a is also produced in Figure S2, but with f replaced by the Coriolis parameter at 40°N (i.e., a constant). The highest values in both cases are found over the midlatitude storm-track regions as expected [cf. *Hoskins and Hodges*, 2002, 2005]. In the NH, the peaks occur on the western side of each basin extending poleward with the general movement of extratropical cyclones [e.g., *Chang et al.*, 2002]. The region with the most frequent occurrence is over the Gulf Stream (GS), where fronts are detected up to a fifth of the time.

However, there are noticeable differences in the structure of the NH storm-track between the two diagnostics. For example, in the North Pacific at 900 hPa, while the basin-wide structure is relatively similar, the area-averaged F climatology identifies frontal grid points roughly 3% more of the time. Another difference is observed in the GS region; the T diagnostic contour maximum follows closely the position of the GS, whereas for the F diagnostic the frequency structure is broader with maxima closer to the coastline. Most likely this is due to 900 hPa often being within the boundary layer in this region, resulting in an increased influence of the strong GS sea surface temperature (SST) gradient on the solely thermal T diagnostic. It is likely that the influence of strong SST gradients on the differences between the two diagnostics may also contribute to the

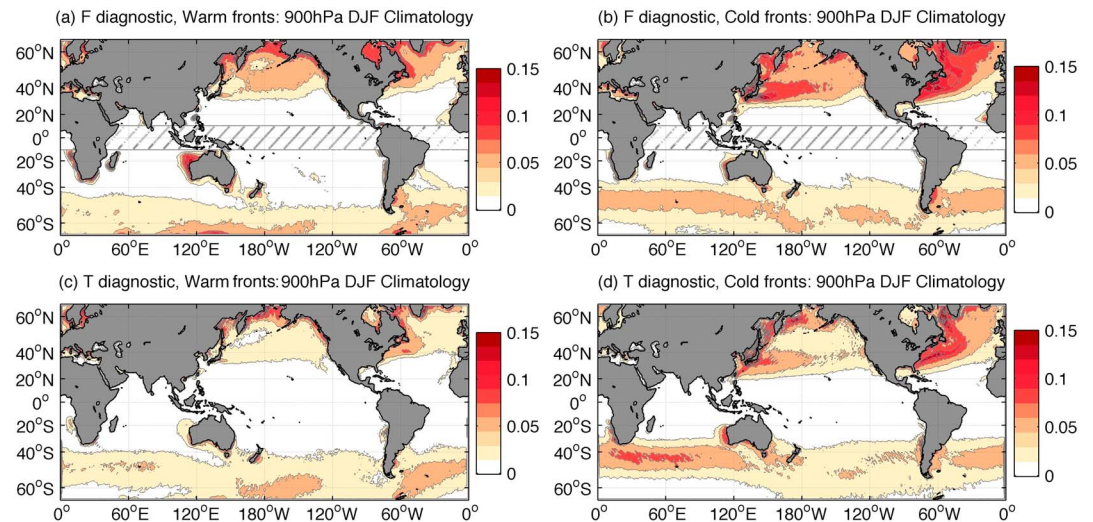


Figure 4. The frequency of warm and cold fronts at 900 hPa, detected using the (a and b) *F* diagnostic and (c and d) *T* diagnostic, for the Northern Hemisphere wintertime period December–February 1979–2015, expressed as a fraction of the total period.

different maxima in the austral summertime storm-track below the southern tips of South Africa and New Zealand.

This supposition is further backed up by consideration of the DJF climatology at 600 hPa for the *F* diagnostic and the *T* diagnostic in Figures 3a and 3b, respectively. At this level, there is a much higher degree of correspondence in structure in these regions of high SST gradient. However, although the structures are more similar, in the western half of both the North Atlantic and North Pacific, the magnitude of frontal frequency calculated with the *F* diagnostic is roughly 3% higher than with the *T* diagnostic. In the eastern half, it is the *T* climatology that exhibits the higher frontal frequency. In the Southern Hemisphere, there is good agreement in the location and structure of the frontal frequency, although it is slightly higher (~1–2%) in the *T* climatology. Another important observation is that in both cases there are much fewer fronts identified around coastlines at 600 hPa. This is due to the reduced influence of the land-sea contrast outside of the atmospheric boundary layer on both temperature gradients and relative vorticity anomalies.

It is noted that the differences between the two diagnostics discussed in this section are relevant for identification of both cold and warm frontal regions individually. To illustrate this, a 900 hPa DJF climatology is shown for warm (Figures 4a and 4c) and cold (Figures 4b and 4d) fronts separately in Figure 4, for both the *F* (Figures 4a and 4b) and *T* (Figures 4c and 4d) diagnostics. It is emphasized, however, that within a particular diagnostic, one does not expect the cold and warm frontal frequencies to be equal. Over the NH western boundary currents, for example, the cold frontal frequency is up to 100% larger than the warm frontal frequency in both diagnostics. It has been suggested that one possible explanation for this could be the relative orientation of cold and warm fronts with the underlying SST gradient [Czaja, 2012; Parfitt *et al.*, 2016].

Lastly, the climatology at 900 hPa and 600 hPa presented in this section is for the DJF season, and so the regions of frontal maxima will strongly reflect the average Northern (Southern) Hemisphere wintertime (summertime) storm-track location. For reference, an analogous climatology is produced for the June–August (JJA) season in Figure S3 for 900 hPa and Figure S4 for 600 hPa.

5. Conclusions

A robust frontal identification method (the *F* diagnostic), in which fronts are identified as regions where the normalized product of the isobaric relative vorticity and horizontal temperature gradient exceed a threshold value, has been introduced. Through analysis of a case study and calculation of seasonal climatology, it has been compared with the more traditional thermal detection method outlined in H98 (the *T* diagnostic). It is noted that the inclusion of both a thermal and dynamical component in the *F* diagnostic results in a method

of reduced mathematical and computational complexity in comparison to the T diagnostic. In the case study, fronts embedded within an extratropical cyclone were objectively detected as expected, with both diagnostics showing a high degree of agreement. Nonetheless, some noticeable differences were observed, although these were often in regions where the identification as “frontal” was more subject to interpretation. These differences were especially apparent for frontal regions of little contiguous extension.

As a result, a minimum of two neighboring points was imposed as in *Smirnov et al.* [2015] in the calculation of the DJF frontal climatology at both 900 hPa and 600 hPa, shown in section 4. At 900 hPa, both diagnostics identified the major storm-track regions as expected, although there were significant differences in structure. These were attributed in part to the influence of strong SST gradients and coastlines on the atmospheric boundary layer. Above the boundary layer at 600 hPa, both diagnostics exhibited more similarity in these regions, although the absolute magnitudes of frontal detection varied by up to 3%. These regional differences were present in the climatology for both cold and warm fronts separately. For reference, a JJA frontal climatology was also produced at both 900 hPa and 600 hPa.

The disagreements observed in the identification of frontal regions between the F and T diagnostics highlight an important aspect of objective frontal identification, in that there is no defined “truth” against which one can absolutely test the accuracy of any particular method. In fact, differences between alternative methods are commonplace [e.g., *Hope et al.*, 2014; *Schemm et al.*, 2015], and it is likely that “meteorologists will probably always disagree over the details of a drawn objective front” [*McCann and Whistler*, 2001]. Research is currently taking place by the authors to assess the impact of these differences on both local- and large-scale climate analyses.

Acknowledgments

R.P. is funded by the Weston Howland Jr. postdoctoral scholarship at the Woods Hole Oceanographic Institution. H.S. is grateful for support from NSF under AGS-1355339 and OCE-1419235. ERA-Interim is a public data set and is accessible online at <http://apps.ecmwf.int/datasets/>. We would like to thank the ECMWF for allowing access to the ERA-Interim data set. We are grateful for the constructive comments of two anonymous reviewers that have helped improve the paper.

References

- Berrisford, P., D. P. Dee, K. Fielding, M. Fuentes, P. Kallberg, S. Kobayashi, and S. Uppala (2009), The ERA-Interim archive, *ERA Rep. Ser.*, (1), 1–16.
- Berry, G., M. J. Reeder, and C. Jakob (2011a), A global climatology of atmospheric fronts, *Geophys. Res. Lett.*, *38*, L04809, doi:10.1029/2010GL046451.
- Berry, G., C. Jakob, and M. Reeder (2011b), Recent global trends in atmospheric fronts, *Geophys. Res. Lett.*, *38*, L21812, doi:10.1029/2011GL049481.
- Bjerknes, J., and H. Solberg (1922), Life cycles of cyclones and the polar front theory of atmospheric circulation, *Geofysiske Publikasjoner.*, *3*, 1–18.
- Booth, J. F., L. Thompson, J. Patoux, and K. A. Kelly (2012), Sensitivity of midlatitude storm intensification to perturbations in the sea surface temperature near the Gulf Stream, *Mon. Weather Rev.*, *140*(4), 1241–1256.
- Catto, J. L., and S. Pfahl (2013), The importance of fronts for extreme precipitation, *J. Geophys. Res. Atmos.*, *118*, 10,791–10,801, doi:10.1002/jgrd.50852.
- Catto, J. L., C. Jakob, G. Berry, and N. Nicholls (2012), Relating global precipitation to atmospheric fronts, *Geophys. Res. Lett.*, *39*, L10805, doi:10.1029/2012GL051736.
- Chang, E. K., S. Lee, and K. L. Swanson (2002), Storm track dynamics, *J. Clim.*, *15*(16), 2163–2183.
- Clarke, L. C., and R. J. Renard (1966), The U.S. Navy numerical frontal analysis scheme: Further development and a limited evaluation, *J. Appl. Meteorol.*, *5*(6), 764–777.
- Czaja, A. (2012), Ocean-atmosphere coupling in midlatitudes: Does it invigorate or damp the storm track? ECMWF workshop, reading, U. K. [Available at <http://www.ecmwf.int/sites/default/files/elibrary/2013/8850-ocean-atmosphere-coupling-mid-latitudes-does-it-invigorate-or-damp-storm-track.pdf>.]
- Hawcroft, M. K., L. C. Shaffrey, K. I. Hodges, and H. F. Dacre (2012), How much Northern Hemisphere precipitation is associated with extratropical cyclones?, *Geophys. Res. Lett.*, *39*, L24809, doi:10.1029/2012GL053866.
- Hewson, T. D. (1998), Objective fronts, *Meteorol. Appl.*, *5*(01), 37–65.
- Hope, P., et al. (2014), A comparison of automated methods of front recognition for climate studies: A case study in southwest Western Australia, *Mon. Weather Rev.*, *142*(1), 343–363.
- Hoskins, B. J. (1982), The mathematical theory of frontogenesis, *Annu. Rev. Fluid Mech.*, *14*(1), 131–151.
- Hoskins, B. J., and K. I. Hodges (2002), New perspectives on the Northern Hemisphere winter storm tracks, *J. Atmos. Sci.*, *59*(6), 1041–1061.
- Hoskins, B. J., and K. I. Hodges (2005), A new perspective on Southern Hemisphere storm tracks, *J. Clim.*, *18*(20), 4108–4129.
- Huber-Pock, F., and C. Kress (1981), Contributions to the problem of numerical frontal analysis. in *Proceedings of the Symposium on Current Problems of Weather-Prediction*, Zentralanstalt für Meteorologie und Geodynamik, 253, Vienna, 23–26 June.
- Huber-Pock, F., and C. Kress (1989), An operational model of objective frontal analysis based on ECMWF products, *Meteorol. Atmos. Phys.*, *40*(4), 170–180.
- Japan Meteorological Agency (1988), On the improvement of the significant weather chart, *Weather Serv. Bull.*, *55*, 1–16.
- Jenkner, J., M. Sprenger, I. Schwenk, C. Schwierz, S. Dierer, and D. Leuenberger (2010), Detection and climatology of fronts in a high-resolution model reanalysis over the Alps, *Meteorol. Appl.*, *17*(1), 1–16.
- McCann, D. W., and J. P. Whistler (2001), Problems and solutions for drawing fronts objectively, *Meteorol. Appl.*, *8*(2), 195–203.
- Neu, U., et al. (2013), IMILAST: A community effort to intercompare extratropical cyclone detection and tracking algorithms, *Bull. Am. Meteorol. Soc.*, *94*(4), 529–547.
- Parfitt, R. (2014), Extreme air-sea interactions over the Gulf Stream, PhD thesis, 189 pp., Imperial College, London.
- Parfitt, R., A. Czaja, S. Minobe, and A. Kuwano-Yoshida (2016), The atmospheric frontal response to SST perturbations in the Gulf Stream region, *Geophys. Res. Lett.*, *43*, 2299–2306, doi:10.1002/2016GL067723.

- Parfitt, R., A. Czaja, and Y. O. Kwon (2017). The impact of SST resolution change in the ERA-Interim reanalysis on wintertime Gulf Stream frontal air-sea interaction, *Geophys. Res. Lett.*, *44*, 3246–3254, doi:10.1002/2017GL073028.
- Renard, R. J., and L. C. Clarke (1965), Experiments in numerical objective frontal analysis, *Mon. Weather Rev.*, *93*, 547–556.
- Schemm, S., I. Rudeva, and I. Simmonds (2015), Extratropical fronts in the lower troposphere—Global perspectives obtained from two automated methods, *Q. J. R. Meteorol. Soc.*, *141*(690), 1686–1698.
- Sheldon, L. (2015), The role of the deep moist convective processes in western boundary currents-troposphere coupling, PhD thesis, 229 pp., Imperial College, London.
- Simmonds, I., K. Keay, and J. A. Tristram Bye (2012), Identification and climatology of Southern Hemisphere mobile fronts in a modern reanalysis, *J. Clim.*, *25*(6), 1945–1962.
- Smirnov, D., M. Newman, M. A. Alexander, Y. O. Kwon, and C. Frankignoul (2015), Investigating the local atmospheric response to a realistic shift in the Oyashio sea surface temperature front, *J. Clim.*, *28*(3), 1126–1147.



Geophysical Research Letters

Supporting Information for

A simple diagnostic for the detection of atmospheric fronts

Rhys Parfitt^{1,2}, Arnaud Czaja² and Hyodae Seo¹

¹Woods Hole Oceanographic Institution, Woods Hole, USA

²Department of Physics, Imperial College London, UK

Contents of this file

Figures S1 to S4

Introduction

This file contains Supplementary Figures 1-4, along with the associated captions.

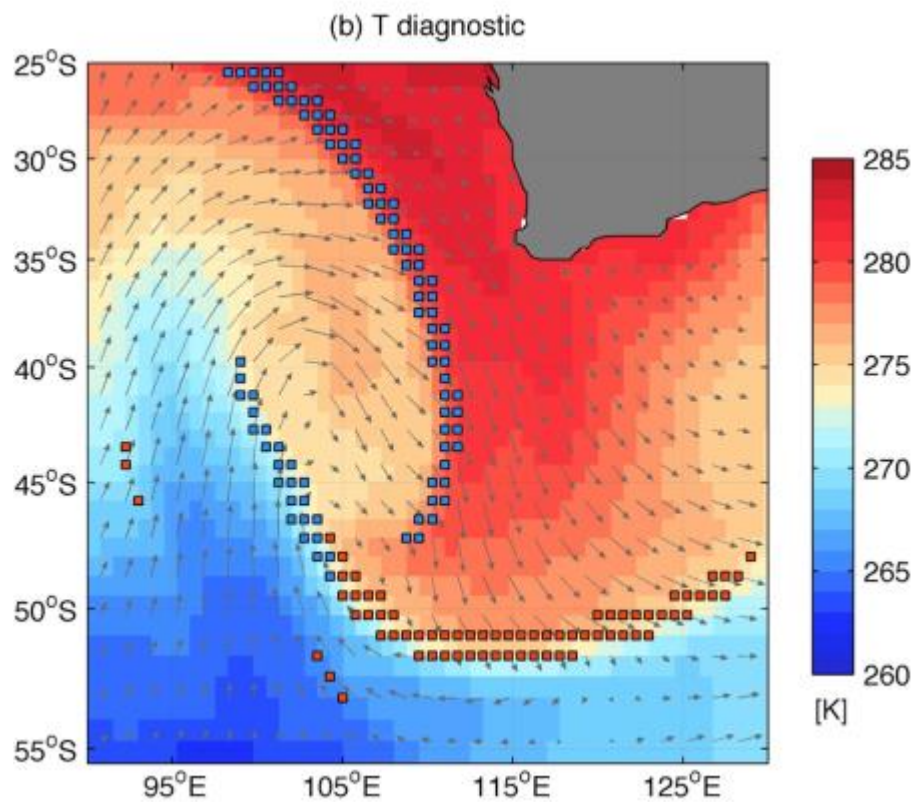
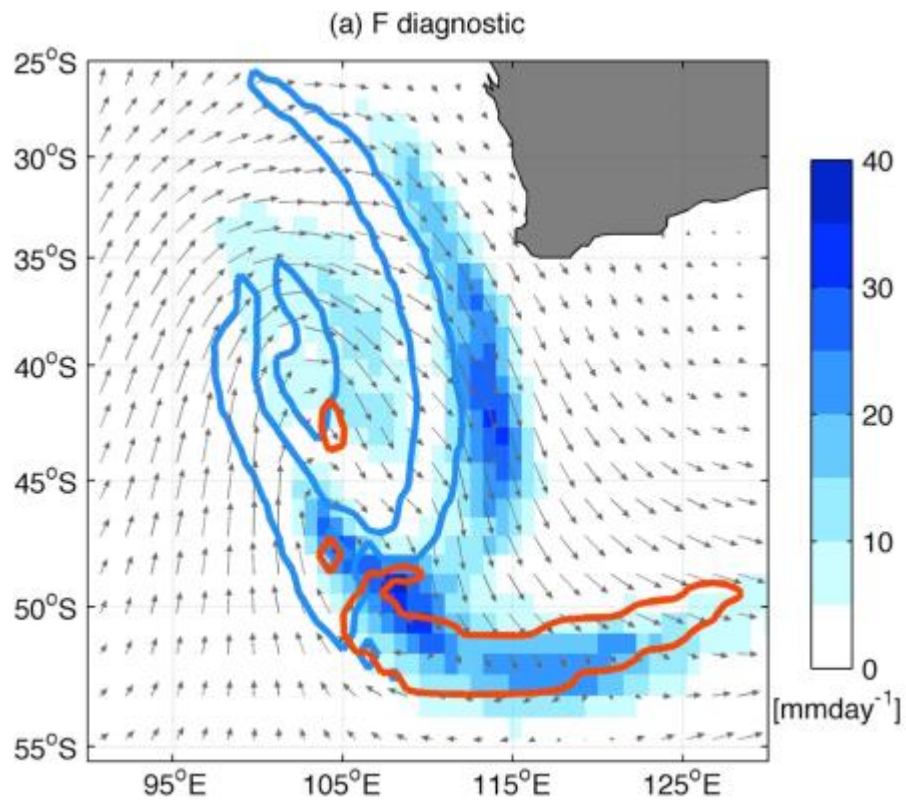


Figure S1: As in Figure 1, except for an extra-tropical cyclone detected in the Southern Hemisphere at 0000UTC on 6th August 1981.

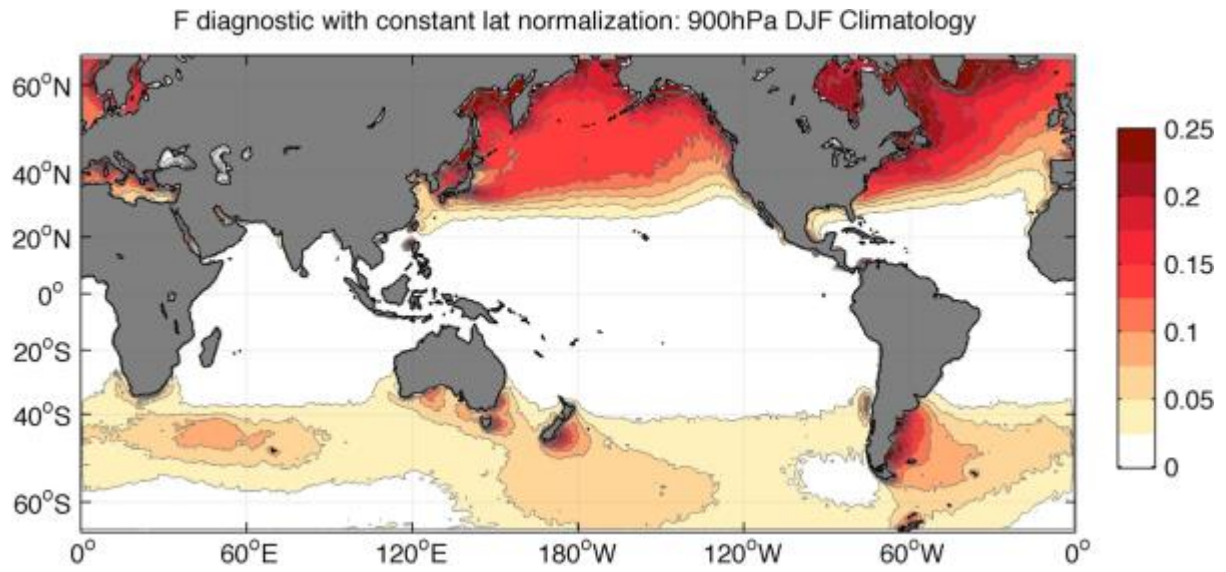


Figure S2: The frequency of all atmospheric fronts at 900hPa detected by a modified ' F ' diagnostic, where f is replaced with a constant equal to the Coriolis parameter at 40°N, expressed as a fraction of the Northern Hemisphere wintertime period December-February 1979-2015.

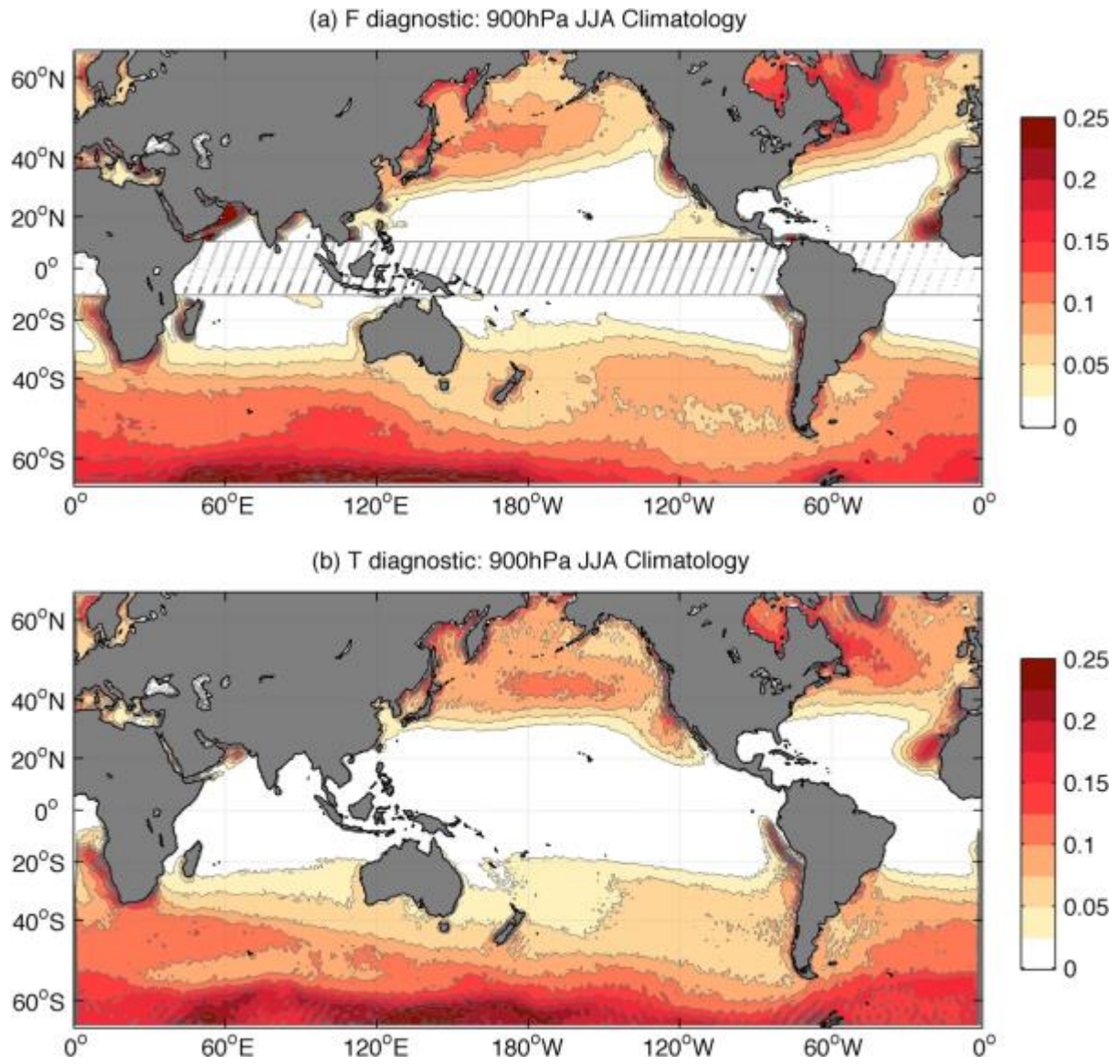


Figure S3: The frequency of all atmospheric fronts at 900hPa detected using the (a) ' F ' diagnostic and (b) ' T ' diagnostic, for the Southern Hemisphere wintertime period June-August 1979-2015, expressed as a fraction of the total period.

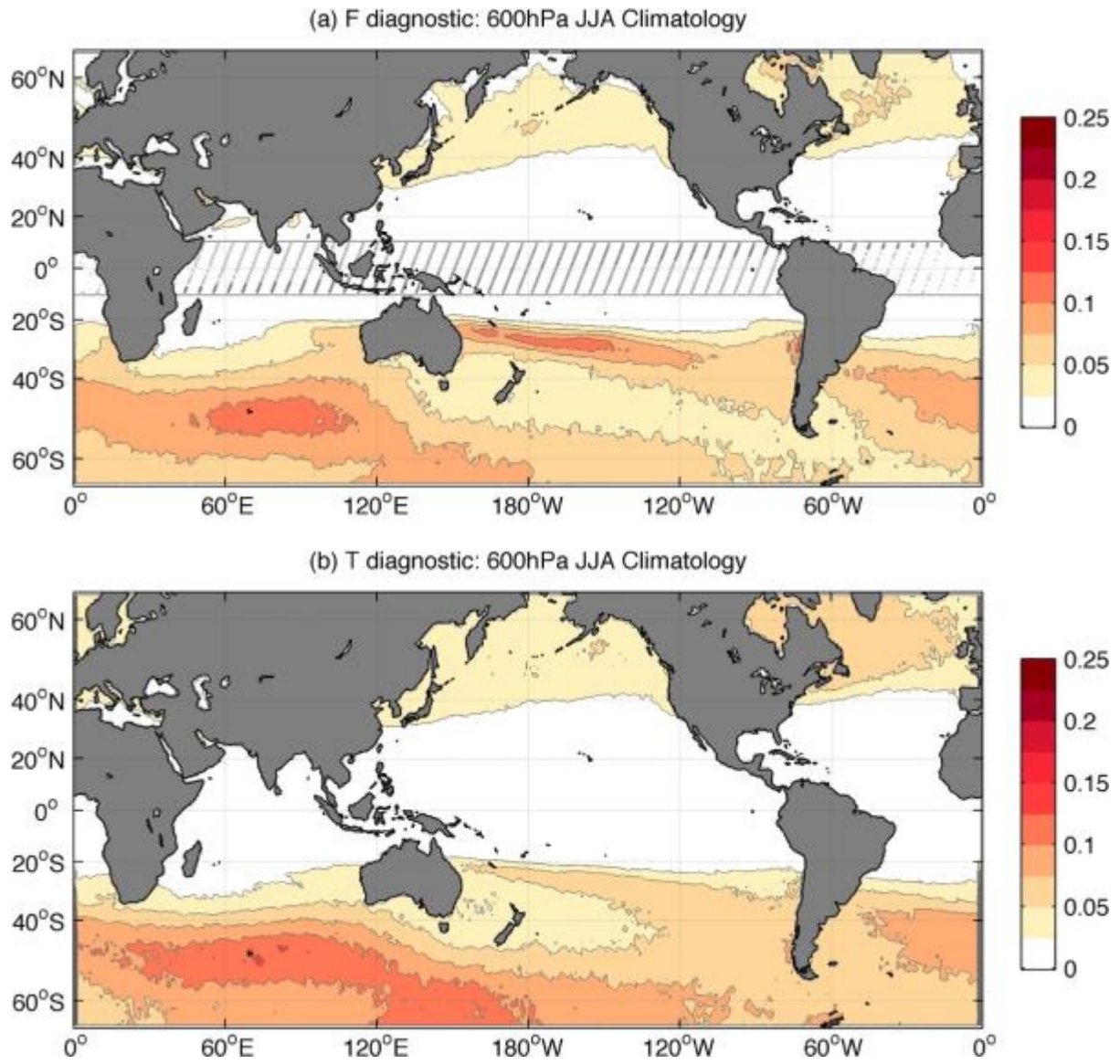


Figure S4: The frequency of all atmospheric fronts at 600hPa detected using the (a) ' F ' diagnostic and (b) ' T ' diagnostic, for the Southern Hemisphere wintertime period June-August 1979-2015, expressed as a fraction of the total period.